Editors' Suggestion

Turbulent lithosphere deformation in the Tibetan Plateau

Xing Jian (简星),[1] Wei Zhang (张巍),[1] Qiang Deng (邓强),[1] and Yongxiang Huang (黄永祥)[1,2,*]
[1]*State Key Laboratory of Marine Environmental Science, College of Ocean and Earth Sciences, Xiamen University, Xiamen 361102, China*
[2]*Fujian Engineering Research Center for Ocean Remote Sensing Big Data, Xiamen, China" for Yongxiang Huang*

(Received 20 January 2019; published 21 June 2019)

In this work, we show that the Tibetan Plateau deformation demonstrates turbulence-like statistics, e.g., spatial invariance across continuous scales. A dual-power-law behavior is evident to show the existence of two possible conservation laws for the enstrophy-like cascade in the range $500 \lesssim r \lesssim 2\,000$ km and kinetic-energy-like cascade in the range $50 \lesssim r \lesssim 500$ km. The measured second-order structure-function scaling exponents $\zeta(2)$ are similar to their counterparts in the Fourier scaling exponents observed in the atmosphere, where in the latter case the earth's rotation is relevant. The turbulent statistics observed here for nearly zero-Reynolds-number flow can be interpreted by the geostrophic turbulence theory. Moreover, the intermittency correction is recognized with an intensity close to that of the hydrodynamic turbulence of high-Reynolds-number turbulent flows, implying a universal scaling feature of very different turbulent flows. Our results not only shed new light on the debate regarding the mechanism of the Tibetan Plateau deformation but also lead to new challenges for the geodynamic modeling using Newton or non-Newtonian models because the observed turbulence-like features have to be taken into account.

DOI: 10.1103/PhysRevE.99.062122

I. INTRODUCTION

The Tibetan Plateau, usually referred to as the "roof of the world," has a double-thickened crust and stands at an average elevation of 5 km over a region of approximately 3 million km^2; see Fig. 1(a). Given the India-Eurasia collision and uplift of the plateau, the most significant geological events on the earth during the Cenozoic time, the Tibetan Plateau has been widely regarded as an ideal field laboratory for understanding the geodynamic processes of continental collision, deformation, and the interactions between uplift and global climate change [1–4]. However, how the Tibetan Plateau deformed and grew remains highly controversial. Proposed hypotheses mainly include (1) rigid plates or blocks northward propagating subduction and extrusion [5,6], (2) convective removal of mantle lithosphere and rapid, continuous, and complete deformation [3], and (3) lower crustal flow rather than substantial upper crustal thickening, which contributes to the plateau deformation and uplift [7,8]. These models are very creative and highly provocative, represent distinct driving mechanisms and kinematic descriptions of surface deformation, and thus have attracted considerable attention for decades. To test these hypotheses, a great number of geological and geophysical data and various methods have been used, primarily including paleoaltimetry, thermochronology, basin analysis and magnetostratigraphy, global positioning system (GPS) data, and subsurface geophysical data analyses [9–15]. Although none of these models account for all of the geological and geophysical data and observations, more studies are aware of the presence of continuous medium and the important role of the rheology in the surface deformation of the Tibetan Plateau [8,9,16]. However, to the best of our knowledge, the spatial scale invariance of such flowing deformation has never been taken into account.

Turbulence or turbulence-like phenomena are ubiquitous in the nature, which is often characterized by scale invariance in both spatial and temporal domains. It ranges from the evolution of the universe [17], movement of atmosphere and ocean [18,19], paintings by Leonardo da Vinci [20] and van Gogh [21], collective motion of bacteria [22,23], and the Bose-Einstein condensate [24] to financial activity [25–29], etc. Note that turbulence is usually recognized by its main features in which a broad range of spatial and temporal scales or many degrees of freedom are excited in the dynamical system [30,31]. The turbulence theory thus describes the energy injection and dissipation patterns or the balance among other physical quantities. This pattern could be quite different for different dynamical systems. For instance, in the classical three-dimensional hydrodynamical turbulence, the energy is injected into the system at a large scale and is transferred to a small scale, and so on, until to the viscosity scale where the kinetic energy is converting to heat [20]. This is a forward energy cascade with the famous Kolmogorov 5/3 law for the spatial Fourier power spectrum of high-Reynolds-number turbulent flows, e.g., $E(k) \propto k^{-5/3}$. While in the two-dimensional turbulence, the energy (resp., enstrophy, square of vorticity) is input into the system through a middle scale. It is then transferred upward (resp., downward) due to energy (resp., enstrophy) conservation with a 5/3 law for a large-scale part (resp., 3 scaling law for small-scale part) [32]. Another famous example is the theory of geostrophic turbulence, in which the horizontal pressure gradient is balanced by the Coriolis force [33]. A potential enstrophy cascade with a scaling exponent 3 (resp., large-scale part) and energy

*yongxianghuang@gmail.com

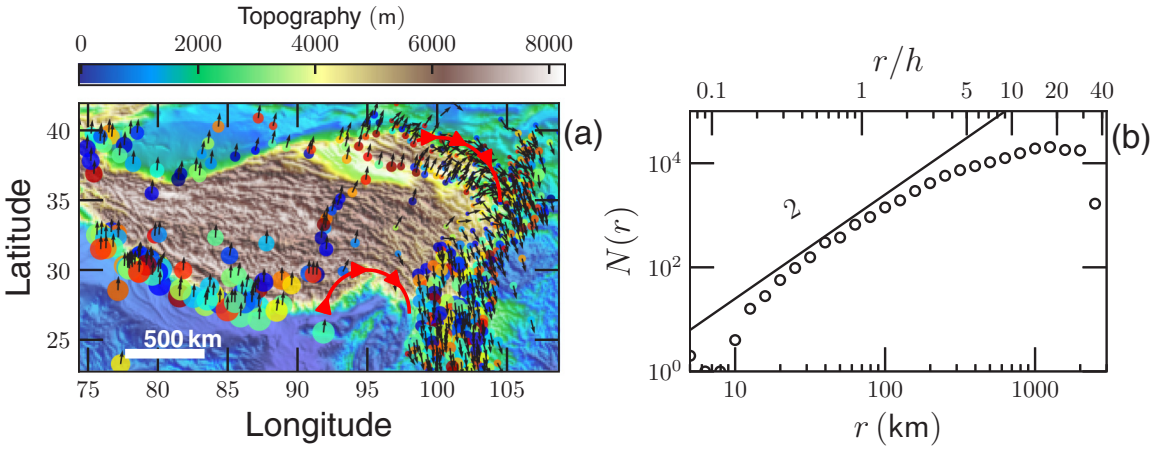

FIG. 1. (a) Spatial distribution of the 553 GPS monitoring stations at the Tibetan Plateau, where the velocity amplitude in cm is encoded by symbol size. The velocity unit vector is indicated by an arrow. Large clockwise rotation of crustal material around the eastern Himalayan syntaxis are illustrated by the big arrow. The GPS velocity data are taken from Ref. [9]. The color map is the elevation provided by ETOPO1 [35]. (b) The experimental number distribution of the neighbor distance, where r is the great circle distance and $h = 70$ km is the average depth of the lithosphere. The solid line indicates a power-law relation with a scaling exponent 2 for reference.

cascade with a scaling exponent 5/3 (small-scale part) are then presented [34].

In this work, in the spirit of the turbulence theory, we show that the Tibetan Plateau deformation also demonstrates turbulence-like statistics, e.g., spatial invariance across continuous scales. A dual-power-law behavior is evident to show the existence of two possible conservation laws for the (potential) enstrophy-like cascade on the range $500 \lesssim r \lesssim 2\,000$ km and kinetic-energy-like cascade on the range $50 \lesssim r \lesssim 500$ km. The measured second-order structure-function (SF) scaling exponents $\zeta(2)$ are similar to the ones observed in the atmosphere [18], where in the latter case the earth's rotation is relevant. The turbulent statistics observed here favor interpretation by the geostrophic turbulence theory, where a large-scale forcing due to the India-Euraisa collision might be balanced by the Coriolis force. Furthermore, the intermittency correction is identified with a strength close to the one of three-dimensional hydrodynamical turbulence of high-Reynolds-number turbulent flows. Our results not only shed new light on the debate regarding the mechanism of the Tibetan Plateau deformation but also lead to new challenges for the geodynamic modeling because the observed turbulent features have to be taken into account.

II. DATA AND METHODOLOGY

The GPS velocity data set is provided in Ref. [9]. Figure 1 shows the deformation velocity unit vector collected from 553 monitoring locations [9], where the topology provided by Earth Topography 1 arc-minute [35] is illustrated in a color map. The symbols indicates the velocity magnitude in the range 0.17–3.95 cm/year. Their mean magnitude and standard deviation respectively are 1.27 and 0.97 cm/year. Figure 1(b) shows the distribution of the neighbor distance of two pairs of monitoring locations. Note that a power-law behavior with a scaling exponent 2 indicates a homogeneous distribution of these monitoring stations, which is illustrated by a solid line for reference in Fig. 1(b). Roughly speaking, the monitoring stations are homogeneously distributed on the scale range $20 \lesssim r \lesssim 200$ km (resp., $0.3 \lesssim r/h \lesssim 3$, where $h = 70$ km is the average depth of the Tibetan lithosphere).

The velocity pattern demonstrates an anticyclone (clockwise) structure, showing eddylike motions. To characterize the motions more quantitatively, we introduce here a second-order moment of the structure function (SF), which is written as

$$S_2(r) = \langle |\mathbf{u}(\mathbf{x}+\mathbf{r}) - \mathbf{u}(\mathbf{x})|^2 \rangle, \tag{1}$$

where $r = |\mathbf{r}|$ is the great circle distance and $\mathbf{u}$ is the velocity vector. For a scaling process, one expects the following relation:

$$S_2(r) \propto r^{\zeta(2)}. \tag{2}$$

Figure 2(a) shows the measured second-order SF $S_2(r)$. A dual-power-law behavior is evident respectively on the range $50 \lesssim r \lesssim 500$ km (resp., $0.7 \lesssim r/h \lesssim 7$) and $500 \lesssim r \lesssim 2\,000$ km (resp., $7 \lesssim r/h \lesssim 28$). The experimental scaling exponents are found to be $\zeta^{\mathrm{S}}(2) = 0.72 \pm 0.07$ and $\zeta^{\mathrm{L}}(2) = 2.50 \pm 0.07$, where the error indicates a 95% fitting confidence level. According to the Wiener-Khinchin theorem, the Fourier power spectrum of the deformation velocity also follows a power-law behavior [20,36],

$$E(k) \propto k^{-\beta}, \quad \beta = 1 + \zeta(2). \tag{3}$$

Thus, the scaling exponent of the Fourier power spectrum indicated by second-order SF are $\beta^{\mathrm{L}} = 3.5$ and $\beta^{\mathrm{S}} = 1.72$, which could be verified in the future when more data are available from either observation or numerical simulation.

III. RESULTS AND DISCUSSION

A. Scaling of deformation

The value of the scaling exponent $\zeta^{\mathrm{S}}(2)$ provided by the second-order SF is close to 2/3, which implies a kinetic energy cascade that has been predicted by several theories, for example, the Kolmogorov 1941 theory for three-dimensional homogeneous and isotropic turbulence for the fully developed hydrodynamic turbulence [20]; the Kraichnan 1967 theory

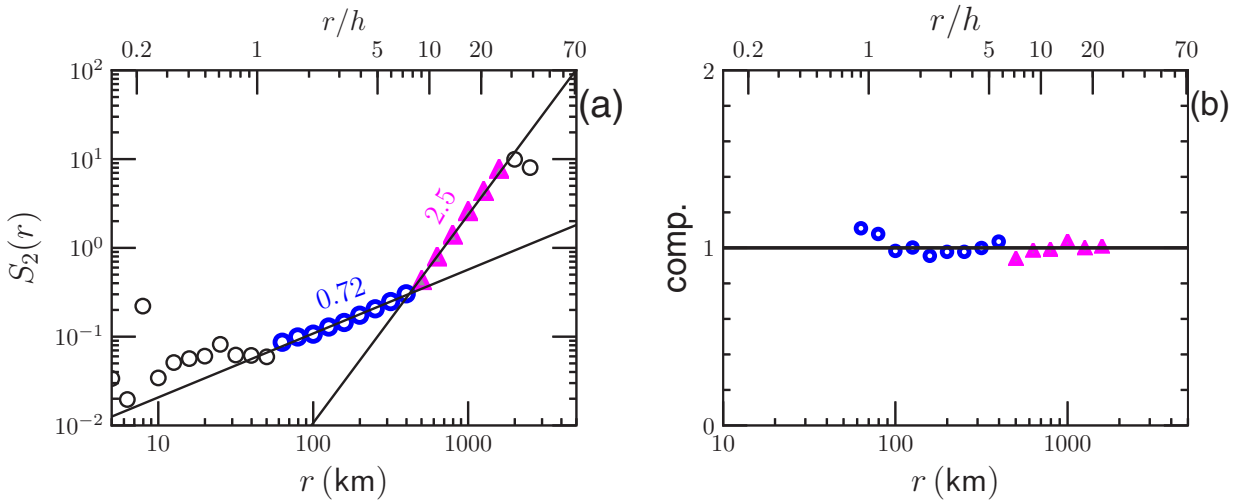

FIG. 2. (a) Measured second-order structure functions. The solid line is the fitting on the range $50 \lesssim r \lesssim 500$ km (resp., $0.7 \lesssim r/h \lesssim 7$) and $500 \lesssim r \lesssim 2\,000$ km (resp., $7 \lesssim r/h \lesssim 28$) with respectively scaling exponent 0.72 ± 0.07 and 2.50 ± 0.07. (b) The corresponding compensated curve, e.g., $S_2(r)r^{-\zeta(2)}C^{-1}$ using a fitted parameter, to highlight the power-law behavior.

for the two-dimensional turbulence [32]; and the Charney 1971 theory for the geostrophic turbulence [33]. The another scaling value $\zeta^{\mathrm{L}}(2)$ may imply a (potential) enstrophy conservation in the framework of two-dimensional turbulence [32] or geostrophic turbulence [33]. As previously mentioned, the mechanism behind the power law is the pattern between injection and dissipation. Therefore, to exclude any possible explanations, the external force that driving the lithosphere deformation has to be recognized. A possible driving force is from the collision between the Indian and Eurasian plates with a large-scale instability above 2000 km. Another possibility for the external force is at scale around 500 km, where the kinetic energy is injected into the system via the thermal plumes of the mantle convection [37]. Because of the complexity of the current problem, such a balanced pattern is more complex than the ideal two-dimensional (2D) turbulence theory or geostrophic turbulence theory. With the limited data, we cannot rule out any one of them. A scale-to-scale energy or enstrophy flux should be checked with attention to identify the cascade direction when the data are available [31,38].

It is interesting to note that a similar dual-power-law behavior has been reported for the atmospheric movement in the Fourier space with the same separation scale around 500 km around the same latitude [18,39], where the separation scale 500 km is determined by geostrophic balance that is described by the Rossby number; see the definition below. According to Vallgren *et al.* [34], if the large-scale forcing due to the India-Eurasia collision is applicable, then the geostropic turbulence is favorable. Note that the power-law behavior observed here is consistent with the discovery of the continuous deformation by Zhang *et al.* [9] for the spatial scale above 100 km.

The basic characteristic of turbulent systems is intermittency, manifested as intense and sporadic fluctuations on different scales of motion. It is one of the most fascinating features of hydrodynamic turbulence [20], which has been reported also for other complex dynamic systems [40]. To track such intermittency correction, a high-order SFs is introduced, i.e.,

$$S_q(r) = \langle |\mathbf{u}(\mathbf{x}+\mathbf{r}) - \mathbf{u}(\mathbf{x})|^q \rangle \propto r^{\zeta(q)} \tag{4}$$

where $\zeta(q)$ is the scaling exponents for high-order SFs. $\zeta(q)$ is linear with q if there is no intermittency correction and vice versa. The deviation from linear relation is usually believed to be an effect of the nonlinear interactions between different scales [20], manifesting as a large variation of the considered data [40]. Note that the $S_q(r)$ can be also defined via a r- dependent probability density function (pdf) $p(\Delta u_r)$ of velocity difference $\Delta u_r = \mathbf{u}(\mathbf{x}+\mathbf{r}) - \mathbf{u}(\mathbf{x})$,

$$S_q(r) = \langle |\Delta u_r|^q \rangle = \int p(\Delta u_r)|\Delta u_r|^q \, \mathrm{d}\Delta u_r \tag{5}$$

where $p(\Delta u_r)|\Delta u_r|^q$ is the qth-order integral kernel. To check whether the statistics is convergent, we plot the measured pdf and the corresponding integral kernel in Fig. 3 for (a) $50 \lesssim r \lesssim 500$ km and (b) $500 \lesssim r \lesssim 2\,000$ km. It suggests a safe estimation of the high-order SFs on the range $-1 \leqslant q \leqslant 4$ with this limit data set.

High-order SFs are then calculated with $-1 \leqslant q \leqslant 4$. However, only the case for $0 \leqslant q \leqslant 4$ is discussed below. Figure 4(a) shows the SFs for $q = 1$ (◯), 3 (□), and 4 (△), where the solid line is a least square fitting. The dual power law is evident on the same scale ranges. Figure 4(b) shows the corresponding compensated curves to highlight the observed power-law behavior. Figure 5(a) shows the measured scaling exponents for small-scale part $\zeta^{\mathrm{S}}(q)$ (◯) and large-scale one $\zeta^{\mathrm{L}}(q)$ (□). For comparison, $\zeta(q) = q/3$ for the energy cascade and $\zeta(q) = q$ for the (potential) enstrophy cascade are also shown. First of all, the experimental curves are convex, confirming the existence of intermittency correction. Second, the scaling exponent $\zeta^{\mathrm{S}}(q)$ for the scale on the range $50 \lesssim r \lesssim 500$ km is close to the value $\zeta(q) = q/3$, indicating an energy cascade with intermittency correction. Third, the scaling exponent $\zeta^{\mathrm{L}}(q)$ for the scale on the range $500 \lesssim r \lesssim 2\,000$ km close to the value $\zeta(q) = q$, indicating a (potential) enstrophy cascade with intermittency correction.

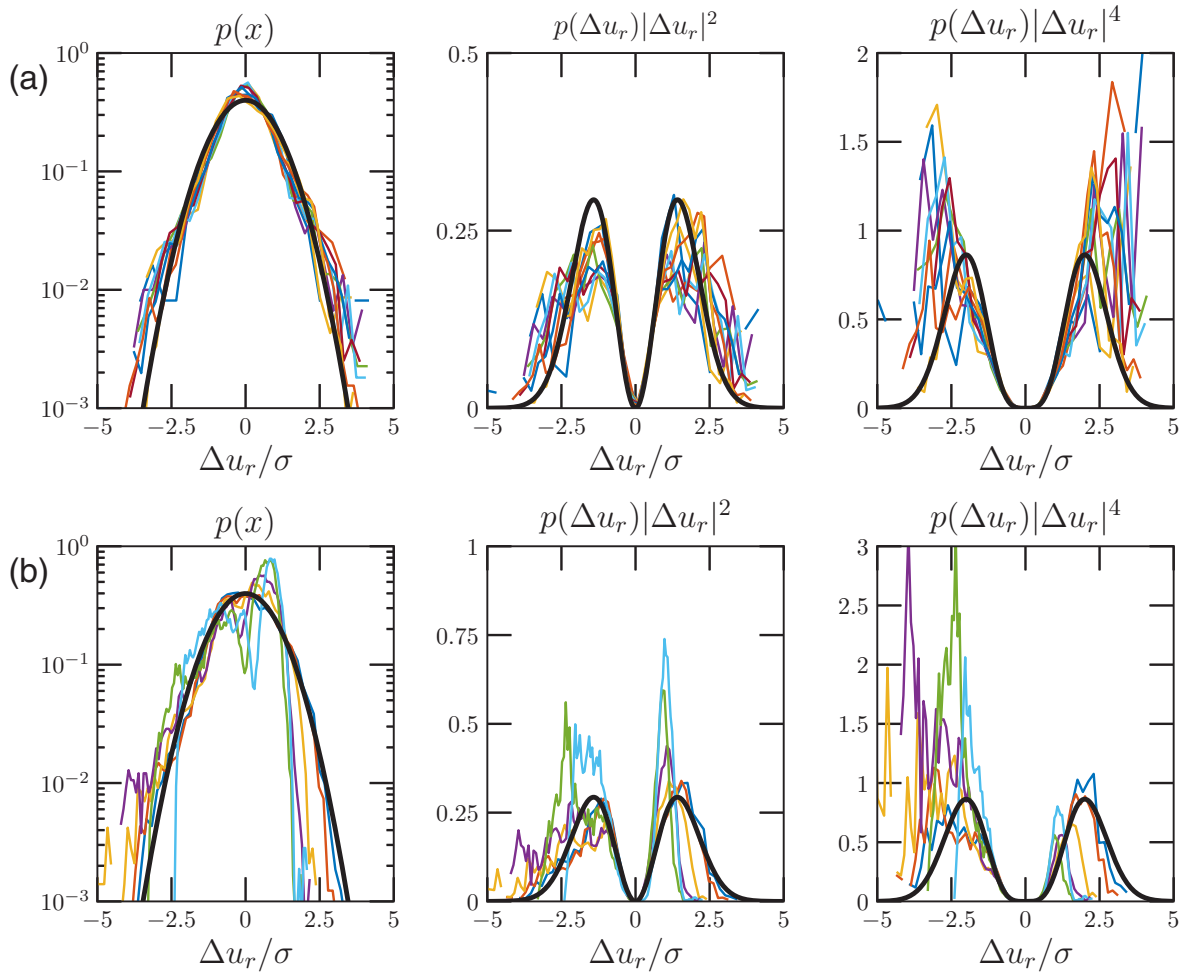

FIG. 3. Experimental probability density function $p(x)$ and the corresponding integral kernel $p(\Delta u_r)|\Delta u_r|^q$ for various separation scales r: (a) $50 \lesssim r \lesssim 500$ km, and (b) $500 \lesssim r \lesssim 2\,000$ km, where the thin line with different color indicates different separation scales and the thick solid line is the normal distribution for reference. Because of the finite sample size, the fourth-order structure function slightly deviates from statistical convergence.

To characterize the intensity of intermittency, the extended self-similarity [43] is plotted as $\zeta_{\mathrm{E},1}(q) = \zeta(q)/\zeta(1)$ versus q; see Fig. 5(b). The experimental curves $\zeta^{\mathrm{S}}_{\mathrm{E},1}(q)$ and $\zeta^{\mathrm{L}}_{\mathrm{E},1}(q)$ collapse with each other when $0 \leqslant q \leqslant 3$. The former one is slightly above the latter one when $3 \leqslant q \leqslant 4$. For comparison, the scaling value of the hydrodynamical turbulence (thick solid line) [41] and passive scalar turbulence (thin solid line) [42] are also illustrated. Graphically, the measured scaling exponents are close to those of hydrodynamical turbulence of high-Reynolds-number turbulent flows, implying a possible universal feature of very different turbulent systems [44].

B. Scaling of topography

To cross verify the above observation, the topography of the Tibetan Plateau provided by ETOPO1 is analyzed below [45]. The evolution of the elevation can be approximately written as

$$h(x,t) = \int_0^t v_h(x,t')dt' \simeq \tilde{v}_h(x)t + h(x,0), \tag{6}$$

where $h(x,t_0)$ is the initial elevation, and the typical vertical velocity $\tilde{v}_h(x)$ can be treated as average vertical velocity since it is a very slowly variation with time. The elevation difference is thus an approximation of the velocity difference,

$$\Delta_r h(x,t) \propto \Delta_r \tilde{v}_h(x)t, \tag{7}$$

where $h(r+x,0) - h(x,0) \ll \{\tilde{v}_h(x+r) - \tilde{v}_h(x)\}t$ is assumed when r is smaller than a certain value, e.g., 500 km. High-order SFs, e.g., $S_q(r) = \langle|\Delta_r h|^q\rangle$ are estimated. A single power-law behavior is observed on the scale range $50 \lesssim r \lesssim 500$ km (resp., $0.7 \lesssim r/h \lesssim 7$) in Fig. 6(a). The measured second-order SF scaling exponent $\zeta(2)$ is to be $\zeta(2) = 0.77 \pm 0.07$, which agrees well with the one of the horizontal deform velocity obtained on the same scale range. Figure 6(b) shows the corresponding compensated curve to emphasize the observed scaling behavior. The measured high-order scaling exponent $\zeta(q)$ with $0 \leqslant q \leqslant 4$ is also shown in Fig. 5 as $\triangle$. Graphically, it agrees well with the one of the horizontal velocity, confirming the existence of the turbulence-like dynamics.

C. Several key parameters

Finally, several possible relevant parameters are discussed as following. A scale-dependent Reynolds number can be

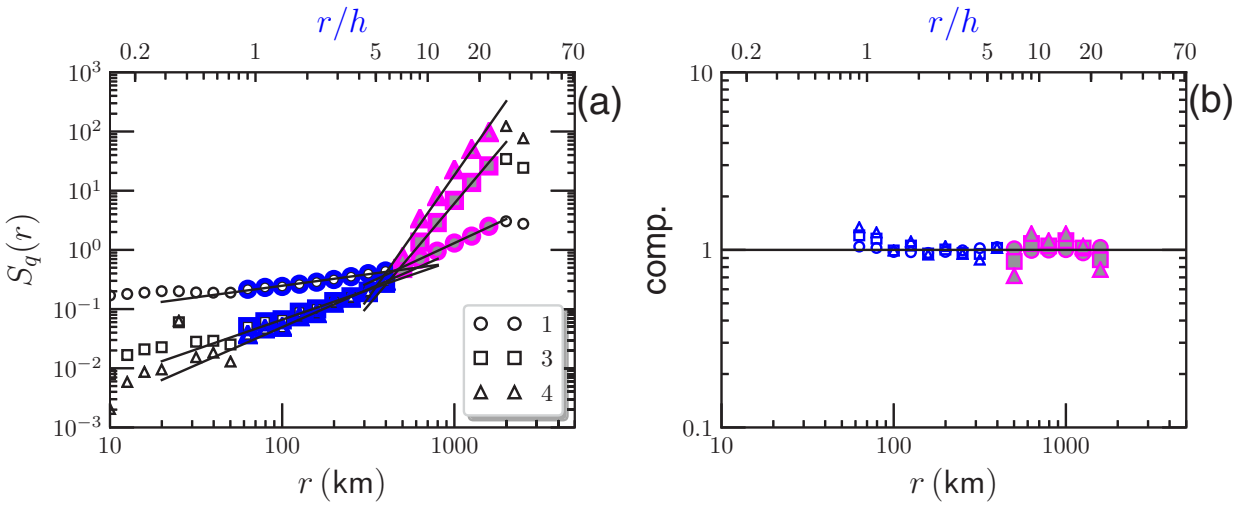

FIG. 4. (a) Measured high-order structure functions $S_q(r)$ for $q = 1, 3, 4$. The solid line illustrates the power-law fitting. (b) The corresponding compensated curve to highlight the power-law behavior.

defined as

$$\mathrm{Re}(r) = \frac{\rho u r}{\mu}, \tag{8}$$

where ρ is the density, u is the velocity, r is the spatial scale, and μ is the dynamic viscosity. It characterizes the ratio between the inertia and viscosity forces. Typical values in Tibet are $\rho \simeq 3\,\mathrm{g/cm^3}$ [46], $u \simeq 1.27\,\mathrm{cm/year}$ [9], and $\mu = 10^{19}$–$10^{24}\,\mathrm{Pa\,s}$ [47], respectively. Considering the spatial scale r from 50 to 2 000 km, one has a Reynolds number in the range $2.4 \times 10^{-24} \lesssim \mathrm{Re}(r) \lesssim 6 \times 10^{-21}$, suggesting that the viscosity force is more relevant than the inertial one in the current problem. Note that turbulence is usually associated with the high-Reynolds-number flows, where the inertia of fluid is relevant and the viscosity force can be neglected [20]. Turbulence without inertia [48] have been reported for the bacterial turbulence [22,23,44], elastic turbulence [30,49], etc., with nearly zero Reynolds number. As aforementioned, the balance pattern could be quite different from the classical hydrodynamic turbulence. However, they might share the universal turbulent features, such as the same strength of the intermittency [44].

Because of the earth's rotation, the Coriolis force could be important. A scale-dependent Rossby number is introduced to characterize this effect, which is written as

$$\mathrm{Ro}(r) = \frac{u}{2\Omega \sin(\phi) r}, \tag{9}$$

where $2\Omega \sin(\phi)$ is the so-called Coriolis frequency, $\Omega = 7.27 \times 10^{-5}\,\mathrm{rad/s}$ is the angular frequency of planetary rotation, and $\phi \simeq 30\,\mathrm{deg}$ is the latitude. It measures the ratio between the inertial force and Coriolis force. Taking the same

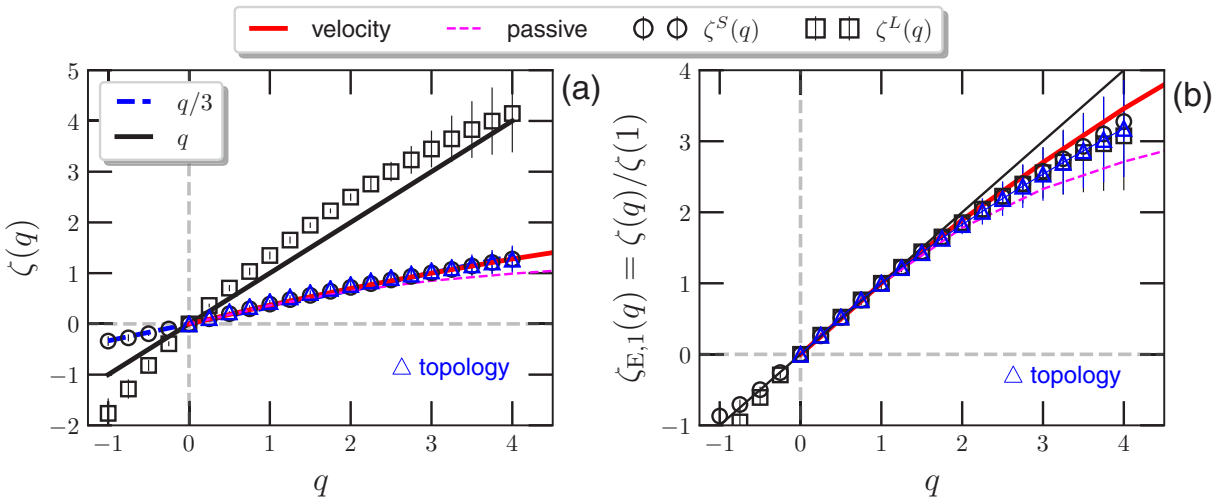

FIG. 5. (a) Measured high-order scaling exponent $\zeta(q)$ of small-scale (◯) and large-scale (□) motions for $-1 \leqslant q \leqslant 4$, where $\zeta(q) = q/3$ (dashed line) and $\zeta(q) = q$ (solid line) are illustrated for reference. (b) The extended self-similarity plot of the measured scaling exponent $\zeta_{E,1}(q) = \zeta(q)/\zeta(1)$. For comparison, the scaling exponents compiled for velocity (thick solid line) [41] and passive scalar (thin solid line) [42] are also shown. The error bar indicates a 95% fitting confidence level. The scaling exponent for topology is illustrated as △.

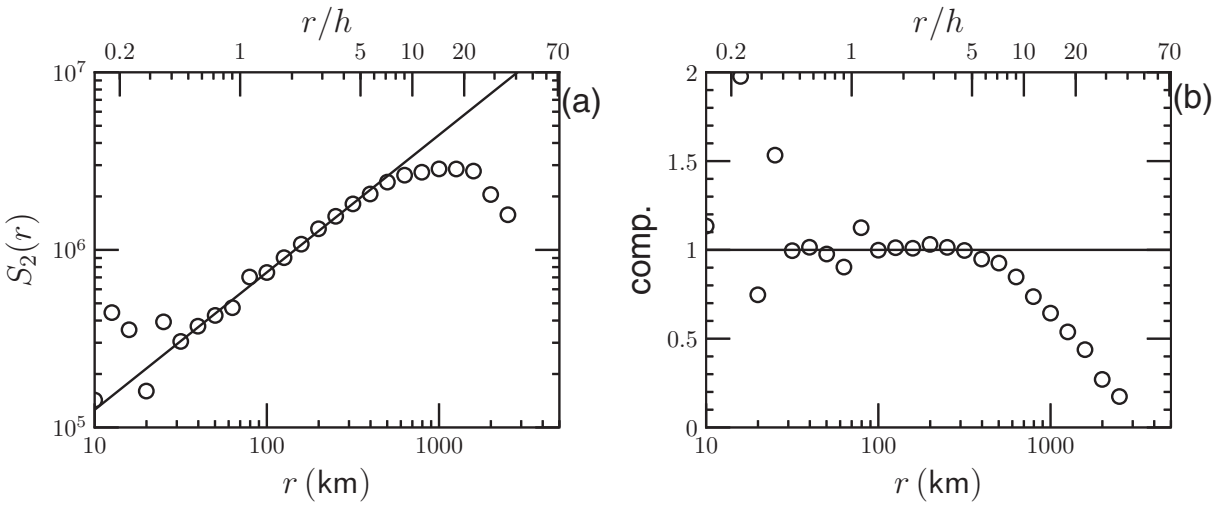

FIG. 6. (a) Experimental second-order structure function for the topography using the ETOPO1 data. Power-law behavior is observed on the range $50 \lesssim r \lesssim 500$ km with a scaling exponent 0.77 ± 0.07. (b) The corresponding compensated curve using fitted parameters to highlight the power-law behavior.

typical velocity and length scales as for the Reynolds number, one has a typical value of $\mathrm{Ro}(r)$ in the range $2.77 \times 10^{-12} \lesssim \mathrm{Ro}(r) \lesssim 1.11 \times 10^{-10}$, implying that the Coriolis force is more relevant than the inertial one.

Finally, a scale-dependent Deborah number is defined as

$$\mathrm{De}(r) = \frac{t_c(r)}{t_p} \tag{10}$$

where $t_c(r)$ refers to the stress relaxation time for a given spatial scale r and t_p is the timescale of observation. It characterizes the ratio of the relaxation time $t_c(r)$, characterizing the time it takes for a material to adjust to applied stresses or deformations and the characteristic timescale t_p of an experiment probing the response of the material. At lower Deborah numbers, the material behaves in a more fluidlike manner, with an associated Newtonian viscous flow. At higher Deborah numbers, the material behavior enters the non-Newtonian regime, increasingly dominated by elasticity and demonstrating solidlike behavior. Typical examples are flows of ice rivers, asphaltum, etc., that over a long time of observation and thus a small Deborah number behave in a fluidlike manner [50]. For the current case, the Deborah number is estimated in the range $0 \leqslant \mathrm{De}(r) \ll 1$, suggesting that the lithosphere deformation can be treated as fluid flow.

IV. CONCLUSION

In summary, in this work, the lithosphere deformation of the Tibetan Plateau is analyzed in the spirit of the multiscale statistics from turbulence community. The dual-power-law behavior is evident respectively on the range $50 \lesssim r \lesssim 500$ km (resp., $0.7 \lesssim r/h \lesssim 7$) and $500 \lesssim r \lesssim 2\,000$ km (resp., $7 \lesssim r/h \lesssim 28$). The scaling feature of the former scaling range indicates an energy cascade, while the one of the latter scaling range implies a (potential) enstrophy cascade, which might be interpreted in the framework of geostrophic turbulence since one possible external force can be identified from the India-Eurasia collision with a spatial scale above 2 000 km. The multiscale feature similar to the one from the atmosphere suggests that they might share similar dynamics, e.g., the balance between large-scale force and Coriolis force. However, to exclude any other possibility, a scale-to-scale energy or enstrophy flux has to be estimated either in Fourier space or the physical domain to determine the cascade direction [31,38]; see the example in Ref. [44]. Moreover, the intermittency is revealed via the high-order SFs. With the help of extended self-similarity, the intensity of intermittency is found to be the same as that of hydrodynamic turbulence of high-Reynolds-number turbulent flows, showing a universal feature of very different turbulent flows, even for nearly zero-Reynolds-number flows [23,30,44,49]. Our results not only shed new light on the understanding of the lithosphere deformation of Tibetan Plateau but also lead to new challenges for geophysical modeling using Newtonian or non-Newtonian fluid models because the observed turbulent features have to be taken into account.

ACKNOWLEDGMENTS

This work is sponsored by the National Natural Science Foundation of China (under Grants No. 11732010 and No. 41806052) and partially by the Fundamental Research Funds for the Central Universities (Grants No. 20720180120, No. 20720180123, and No. 20720170073) and the State Key Laboratory of Marine Environmental Science Internal Research Fund (MEL; Grant No. MELRI1802). We thank J. Q. Zhong and F. G. Schmitt for useful discussions.

The source code and GPS data are available in Ref. [51]. We thank the two anonymous reviewers for their careful reading and insightful comments and suggestions.

[1] T. M. Harrison, P. Copeland, W. S. F. Kidd, and A. Yin, Raising Tibet, Science **255**, 1663 (1992).

[2] M. E. Raymo and W. F. Ruddiman, Tectonic forcing of late cenozoic climate, Nature (London) **359**, 117 (1992).

[3] P. Molnar, P. England, and J. Martinod, Mantle dynamics, uplift of the Tibetan Plateau, and the Indian monsoon, Rev. Geophys. **31**, 357 (1993).

[4] Z. S. An, J. E. Kutzbach, W. L. Prell, and S. C. Porter, Evolution of Asian monsoons and phased uplift of the Himalaya-Tibetan plateau since Late Miocene times, Nature (London) **411**, 62 (2001).

[5] P. Tapponnier, G. Peltzer, A. Y. Le Dain, R. Armijo, and P. Cobbold, Propagating extrusion tectonics in Asia: New insights from simple experiments with plasticine, Geology **10**, 611 (1982).

[6] P. Tapponnier, Z. Q. Xu, F. Roger, B. Meyer, N. Arnaud, G. Wittlinger, and J. S. Yang, Oblique stepwise rise and growth of the Tibet Plateau, Science **294**, 1671 (2001).

[7] L. H. Royden, B. C. Burchfiel, R. W. King, E. Wang, Z. L. Chen, F. Shen, and Y. P. Liu, Surface deformation and lower crustal flow in eastern Tibet, Science **276**, 788 (1997).

[8] M. K. Clark and L. H. Royden, Topographic ooze: Building the eastern margin of Tibet by lower crustal flow, Geology **28**, 703 (2000).

[9] P. Z. Zhang, Z. K. Shen, M. Wang, W. J. Gan, R. Bürgmann, P. Molnar, Q. Wang, Z. J. Niu, J. Z. Sun, J. C. Wu, H. R. Sun, and X. Z. You, Continuous deformation of the Tibetan Plateau from global positioning system data, Geology **32**, 809 (2004).

[10] D. B. Rowley and B. S. Currie, Palaeo-altimetry of the late Eocene to Miocene Lunpola basin, central Tibet, Nature (London) **439**, 677 (2006).

[11] M. K. Clark, K. A. Farley, D. W. Zheng, Z. C. Wang, and A. R Duvall, Early Cenozoic faulting of the northern Tibetan Plateau margin from apatite (U-Th)/He ages, Earth Planet. Sci. Lett. **296**, 78 (2010).

[12] D. H. Bai, M. J. Unsworth, M. A. Meju, X. B. Ma, J. W. Teng, X. R Kong, Y. Sun, J. Sun, L. F. Wang, C. S. Jiang, C. P. Zhao, P. F. Xiao, and M. Liu, Crustal deformation of the eastern Tibetan plateau revealed by magnetotelluric imaging, Nat. Geosci. **3**, 358 (2010).

[13] R. O. Lease, D. W. Burbank, H. P. Zhang, J. H. Liu, and D. Y. Yuan, Cenozoic shortening budget for the northeastern edge of the Tibetan Plateau: Is lower crustal flow necessary? Tectonics **31**, TC3011 (2012).

[14] G. D. Hoke, L. Z. Jing, M. T. Hren, G. K. Wissink, and C. N. Garzione, Stable isotopes reveal high southeast Tibetan Plateau margin since the Paleogene, Earth Planet. Sci. Lett. **394**, 270 (2014).

[15] X. Jian, P. Guan, W. Zhang, H. H. Liang, F. Feng, and L. Fu, Late Cretaceous to early Eocene deformation in the northern Tibetan Plateau: Detrital apatite fission track evidence from northern Qaidam Basin, Gondwana Res. **60**, 94 (2018).

[16] L. H. Royden, B. C. Burchiel, and R. D. van der Hilst, The geological evolution of the Tibetan Plateau, Science **321**, 1054 (2008).

[17] C. H. Gibson, Turbulence in the ocean, atmosphere, galaxy, and universe, Appl. Mech. Rev. **49**, 299 (1996).

[18] G. D. Nastrom, K. S. Gage, and W. H. Jasperson, Kinetic energy spectrum of large- and mesoscale atmospheric processes, Nature (London) **310**, 36 (1984).

[19] S. A. Thorpe, *The Turbulent Ocean* (Cambridge University Press, Cambridge, UK, 2005).

[20] U. Frisch, *Turbulence: The Legacy of A. N. Kolmogorov* (Cambridge University Press, Cambridge, UK, 1995).

[21] J. L. Aragón, G. G. Naumis, M. Bai, M. Torres, and P. K. Maini, Turbulent luminance in impassioned van Gogh paintings, J. Math. Imaging Vision **30**, 275 (2008).

[22] H. H. Wensink, J. Dunkel, S. Heidenreich, K. Drescher, R. E. Goldstein, H. Löwen, and J. M. Yeomans, Meso-scale turbulence in living fluids, Proc. Natl. Acad. Sci. USA **109**, 14308 (2012).

[23] X. Qiu, L. Ding, Y. X. Huang, M. Chen, Z. M. Lu, Y. L. Liu, and Q. Zhou, Intermittency measurement in two-dimensional bacterial turbulence, Phys. Rev. E **93**, 062226 (2016).

[24] N. Navon, A. L. Gaunt, R. P. Smith, and Z. Hadzibabic, Emergence of a turbulent cascade in a quantum gas, Nature (London) **539**, 72 (2016).

[25] S. Ghashghaie, W. Breymann, J. Peinke, P. Talkner, and Y. Dodge, Turbulent cascades in foreign exchange markets, Nature (London) **381**, 767 (1996).

[26] F. G. Schmitt, D. Schertzer, and S. Lovejoy, Multifractal analysis of foreign exchange data, Appl. Stoch. Models Data Anal. **15**, 29 (1999).

[27] T. Lux, Turbulence in financial markets: The surprising explanatory power of simple cascade models, Quant. Finance **1**, 632 (2001).

[28] M. Y. Li and Y. X. Huang, Hilbert-Huang transform-based multifractal analysis of China stock market, Phys. A (Amsterdam, Neth.) **406**, 222 (2014).

[29] B. Mandelbrot and R. L. Hudson, *The Misbehavior of Markets: A Fractal View of Financial Turbulence* (Basic Books, New York, 2007).

[30] A. Groisman and V. Steinberg, Elastic turbulence in a polymer solution flow, Nature (London) **405**, 53 (2000).

[31] A. Alexakis and L. Biferale, Cascades and transitions in turbulent flows, Phys. Rep. **767–769**, 1 (2018).

[32] R. H. Kraichnan, Inertial ranges in two-dimensional turbulence, Phys. Fluids **10**, 1417 (1967).

[33] J. G. Charney, Geostrophic turbulence, J. Atmos. Sci. **28**, 1087 (1971).

[34] A. Vallgren, E. Deusebio, and E. Lindborg, Possible Explanation of the Atmospheric kinetic and Potential Energy Spectra, Phys. Rev. Lett. **107**, 268501 (2011).

[35] https://www.ngdc.noaa.gov/mgg/global.

[36] Y. X. Huang, F. G. Schmitt, Z. M. Lu, P. Fougairolles, Y. Gagne, and Y. L. Liu, Second-order structure function in fully developed turbulence, Phys. Rev. E **82**, 026319 (2010).

[37] J. Q. Zhong and J. Zhang, Thermal convection with a free moving top boundary, Phys. Fluids **17**, 115105 (2005).

[38] Q. Zhou, Y. X. Huang, Z. M. Lu, Y. L. Liu, and R. Ni, Scale-to-scale energy and enstrophy transport in two-dimensional Rayleigh-Taylor turbulence, J. Fluid Mech. **786**, 294 (2015).

[39] S. H. Gao, Y. J. Wang, Y. X. Huang, Q. Zhou, Z. M. Lu, X. Shi, and Y. L. Liu, Spatial statistics of atmospheric particulate matter in China, Atmos. Environ. **134**, 162 (2016).

[40] F. G. Schmitt and Y. X. Huang, *Stochastic Analysis of Scaling Time Series: From Turbulence Theory to Applications* (Cambridge University Press, Cambridge, UK, 2016).

[41] F. G. Schmitt, Linking Eulerian and Lagrangian structure functions scaling exponents in turbulence, Phys. A (Amsterdam, Neth.) **368**, 377 (2006).

[42] F. G. Schmitt, Relating Lagrangian passive scalar scaling exponents to Eulerian scaling exponents in turbulence, Eur. Phys. J. B **48**, 129 (2005).

[43] R. Benzi, S. Ciliberto, R. Tripiccione, C. Baudet, F. Massaioli, and S. Succi, Extended self-similarity in turbulent flows, Phys. Rev. E **48**, R29(R) (1993).

[44] L. P. Wang and Y. X. Huang, Intrinsic flow structure and multifractality in two-dimensional bacterial turbulence, Phys. Rev. E **95**, 052215 (2017).

[45] J. S. Gagnon, S. Lovejoy, and D. Schertzer, Multifractal surfaces and terrestrial topography, Europhys. Lett. **62**, 801 (2003).

[46] H. L. Li, J. Fang, and C. Braitenberg, Lithosphere density structure beneath the eastern margin of the Tibetan Plateau and its surrounding areas derived from GOCE gradients data, Geodesy Geodyn. **8**, 147 (2017).

[47] Y. L. Shi and J. L. Cao, Lithosphere effective viscosity of continental China, Earth Sci. Front. **15**, 82 (2008).

[48] R. G. Larson, Turbulence without inertia, Nature (London) **405**, 27 (2000).

[49] A. Groisman and V. Steinberg, Efficient mixing at low Reynolds numbers using polymer additives, Nature (London) **410**, 905 (2001).

[50] M. Reiner, The Deborah number, Phys. Today **17**(1), 62 (1964).

[51] https://github.com/lanlankai.